Ultrafine Pd nanoparticles supported on zeolite-templated mesocellular graphene network via framework aluminum mediation: An advanced oxygen reduction electrocatalyst

Xuexue Cui[a], Yunshi Xu[a], Leilei Chen[a,b], Mingyu Zhao[a], Shuguang Yang[a], Yi Wang[a,b,*]

[a] Center for Advanced Low-dimension Materials, State Key Laboratory for Modification of Chemical Fibers and Polymer Materials, College of Materials Science and Engineering, Donghua University, Shanghai 201620, China
[b] College of Chemistry, Chemical Engineering and Biotechnology, Donghua University, Shanghai 201620, China

ABSTRACT

Constructing ultrafine and highly dispersive palladium nanoparticles on 3-dimentional hierarchically porous carbon matrix is of great significance to develop high-performance and cost-effective electrocatalysts for fuel cell systems. Herein, a facile and stabilizer-free strategy was exploited to decorate of ultrafine and well-dispersive Pd nanoparticles (~2.8 nm) on mesocellular graphene network (MGN) that was templated by zeolite MCM-22. It was found that optimal oxygen defects in MGN templated by zeolite framework Al sites were contributed to the ultrafine structure. The as-prepared Pd/MGN not only inherited the nanosheet structure of zeolite MCM-22 with hierarchical pores, large surface area and high conductivity, but also exhibited plentiful and accessible catalytic active sites. In comparison with the commercial platinum-carbon (Pt/C) catalyst (20 wt %), Pd/MGN demonstrated lower onset potential (positive shift 9 mV), significantly enhanced mass activity (up to 3.6 fold) and much longer durability for cathodic oxygen reduction reaction. It is believed that this work promises a straightforward method to develop carbon-supported ultrafine nanoparticles for low-cost and highly efficient catalytic applications.

1. Introduction

Rational design and synthesis of advanced electrocatalysts with unprecedented catalytic performance in oxygen reduction reaction (ORR) have been regarded as an effective way to overcome the sluggish cathodic kinetics in fuel cells. Traditionally, platinum (Pt) or Pt-based noble metal catalysts have been deemed as the culmination toward ORR due to their high activity [1,2]. Nevertheless, the rareness, high cost, low stability and also the issue of fuels crossover on Pt-based catalysts seriously hinder their commercialization [3–5]. As such, alternative ORR catalysts such as nonprecious metals [6], transition metals [7], doped carbon materials [8] and metal oxides [9] have been widely investigated with promising advances. However, optimizing their performances with simultaneous low-cost, high-activity and good-stability is still on the way. Among these investigated catalysts, palladium is relatively much cheaper and simultaneously possesses comparable activity as well as superior poisoning tolerance to Pt, which promises a potential candidate to substitute Pt-based catalyst [10,11]. To increase the utilization efficiency of Pd and boost its catalytic activity, great

effort has been devoted to enhance the exposure of surface active sites via decreasing the size or increasing the dispersity of Pd nanoparticles [12–14]. Unfortunately, ultra-small nanoparticles with large surface energy are highly mobile and easily aggregative during synthetic and catalytic processes, which would depress the catalytic efficiency [15]. Although using conductive and porous nanomaterials with large surface area to support palladium nanoparticles (Pd NPs) could retard the aggregation, the intricate processes including the employment of organic stabilizer, low temperature (zero degree), or elaborated precursors are usually involved, which would increase the cost and not be beneficial for the practical applications. What's worse, most of these strategies still suffer from either coarse nanoparticles or non-porous structures with low mass transfer and low availability [16–18]. Thus, there still exists an urgent challenge to facilely fabricate ultrafine Pd NPs supported on porous and conductive nano-framework with large and accessible surface for highly efficient ORR.

In this work, a facile strategy was developed to prepare zeolite-templated mesocellular graphene network (MGN)-supported ultrafine Pd nanoparticles (Pd/MGN), serving as an advanced ORR

electrocatalyst. It was found that framework Al of zeolite MCM-22 acted as a Lewis acid to template the MGN with optimal oxygen defect sites. Accordingly, it guaranteed the formation of ultrafine and well-dispersed Pd NPs on these defect sites via stabilizer-free synthesis. As a result, Pd/ MGN NPs possessed hierarchically porous structure with large surface area, high conductivity, fast mass-transfer, plentiful and accessible active sites, which exhibited remarkably advanced catalytic performances for ORR and was much more superior to the state-of-the-art Pt/C catalyst.

2. Experimental section

2.1. Materials

Pt/C (20 wt%) with a BET specific surface area of 90 m^2/g and a pore size of about 3.5 nm was obtained from Johnson-Matthey Corp. (USA). Potassium tetrachloropalladate (K$_2$PdCl$_4$), Nafion-117 solution (5 wt%) and commercial RuO$_2$ catalyst were bought from Sigma-Aldrich (USA). Graphene oxide nanosheets (GO) and silica nanospheres (SiO$_2$) were obtained from Nanjing XFNANO Materials Tech Co., Ltd. (China). Multiwalled carbon nanotube (MWCNT) was obtained from Chengdu Organic Chemicals Company Ltd. of Chinese Academy of Sciences (China). Sucrose, sulfuric acid, sodium borohydride (NaBH$_4$), sodium hydroxide (NaOH), potassium hydroxide (KOH), methanol, ethanol and other reagents, if not specified, were obtained from Sinopharm Chemical Reagent Co., Ltd (Shanghai, China). All chemicals were used without further purification. Ultrapure water (18 MU cm) was used for all experiments.

2.2. Synthesis

2.2.1. Dealumination of MCM-22
Briefly, 1 g MCM-22 zeolite powder was stirred and refluxed in 50 ml HCl (2 M) for 6 h under 120 °C. After that, dealuminated MCM-22 zeolite was obtained by centrifugation, washing and drying.

2.2.2. Synthesis of MGN
MGN was synthesized by using zeolite MCM-22 as the template. Typically, 2 g zeolite MCM-22 powder was dipped in a solution contained 0.1 mL H$_2$SO$_4$ (95–98%) and 1.45 g sucrose for 6 h, then dried at 160 °C. After that, a mixed solution of 0.06 mL H$_2$SO$_4$ (95–98%) and 0.87 g sucrose was added and stirred for 6 h. Again, the mixture was dried at 160 °C for overnight. The obtained black powder was calcined at 800 °C for 1 h under N$_2$ atmosphere. After removal of the zeolite template from the calcined powder under a solution of NaOH (4 M), MGN were recovered via washing and freeze-drying. For comparisons, porous carbon templated by pristine SiO$_2$ (SiO$_2$-C) and dealuminated MCM-22 was accordingly synthesized via the same procedures.

2.2.3. Oxidation of multiwalled carbon nanotubes (oxidized-mwcnt)
Briefly, 1 g MWCNT was stirred and refluxed in 50 mL concentrated acid (H$_2$SO$_4$: HNO$_3$ = 3 : 1, v/v) for 6 h under 60 °C. After dilution with a large amount of water and repeated washing, oxidized-MWCNT were acquired via freeze-drying.

2.2.4. Reduction of graphene oxide (reduced-go)
The GO was subjected to different reductions via calcination at 200 °C or 800 °C under Ar atmosphere for 1 h.

2.2.5. Synthesis of Pd/MGN and the other carbon-supported Pd nanomaterials
For typical synthesis of Pd/MGN at room temperature, 5 mg MGN was ultrasonically dispersed in 0.25 mL and then 0.03 mL K$_2$PdCl$_4$ solution (0.15 M) was added under continuous ultrasound condition. After 30 min, 0.05 mL of the freshly-prepared NaBH$_4$ (1.0 M) solution with NaOH (1.0 M) was dropwise injected into the above mixture and

stirred for 1 h. Afterward, Pd/MGN (about 6.5 wt% Pd loading) was collected by centrifugation, water-washing and then freeze-drying. Correspondingly, the other carbon-supported Pd nanomaterials including Pd/MWCNT, Pd/oxidized MWCNT, Pd/GO, Pd/reduced-GO and Pd/SiO$_2$-C were synthesized using the same methods but only the different carbon precursors.

2.3. Preparation of modified electrodes and electrochemical tests

Prior to use, glassy carbon disk electrodes were successively polished with 1.0 μm, 0.3 μm and 0.05 μm -Al$_2$O$_3$ powder until a shiny mirror surface was obtained. Then, 15 μL homogeneous catalytic ink, which was prepared by dispersing 2 mg catalytic powder in 32 μL Nafion 117 (5 wt.%), 200 μL ethanol (98 vol.%) and 768 μL water, was dropped on the clean glassy carbon rotating disk electrode (RDE, 5 mm, Pine) and dried at room temperature to obtain the working electrode.

Electrochemical measurements including Cyclic voltammetry (CV), Linear sweep voltammetry (LSV) and Electrochemical impedance spectroscopy (EIS) were performed at a CHI 660E electrochemical workstation (Chenhua Co., Shanghai, China) with a three-electrode system of a KCl saturated Ag/AgCl reference electrode, a platinum wire counter electrode and a modified glassy carbon RDE working electrode. Throughout the testing process, 0.1 M KOH solution was served as electrolyte and deaerated by high purity O$_2$ or N$_2$. CV curves were recorded with a scan rate of 50 mV s^{-1}. LSV curves were obtained at 10 mV s^{-1} with different rotate speeds (400, 800, 1200, 1600 and 2000 rpm) under a potential scan range from −0.8 V to +0.2 V. In the acquired LSV curves, ORR onset potential (Eonset) is the potential at the cross of the tangents just before and after the onset of rise current. The kinetic current was calculated according to the Koutecky-Levich (K–L) equation [19]:

$$\frac{1}{J} = \frac{1}{J_K} + \frac{1}{J_L} = \frac{1}{J_K} + \frac{1}{B\omega^{1/2}} \tag{1}$$

$$B = 0.2nFC_0(D_0)^{2/3}\nu^{-1/6} \tag{2}$$

where J is the measured current density, J$_L$ and J$_K$ are the diffusion- and kinetic-limiting current densities of the ORR. B is the Levich slope which is given by the Eq. (2). n is the number of electrons transferred per oxygen molecule. ω is the angular velocity. F is the faraday constant (96485 C mol^{-1}). ν is the kinetic viscosity (0.01 cm^2 s^{-1}). D$_0$ is the diffusion coefficient of O$_2$ in 0.1 M KOH (1.9 × 10^{-5} cm^2 s^{-1}) and C$_0$ is the bulk concentration of O$_2$ (1.2 × 10^{-6} mol cm^{-3}). The constant 0.2 is adopted when the rotation speed is expressed in rpm.

Tafel curve was plotted with the logarithm (log) value of corrected kinetic current vs. its corresponding potential. EIS tests were carried out at the frequency range from 1 MHz to 0.01 Hz. The applied potential and excitation amplitude were +0.2 V and 5 mV, respectively.

2.4. Characterization

Transmission electron microscopy (TEM), high-resolution TEM (HRTEM), scanning transmission electron microscopy (STEM) and energy-dispersive X-ray (EDX) mappings of the catalysts were performed on a JEM-2100 electron microscope (JEOL, Japan) with an acceleration voltage of 200 kV. Nitrogen adsorption-desorption analysis at 77K was performed on a Tristar 3000 system (Micromeritics, USA). The micropore and meso-macropores size distribution curves was calculated using a NLDFT and DFT methods, respectively. X-ray diffraction (XRD) analysis was acquired on a PANalytical X'pert PRO diffractometer (PANalytical, Netherlands) equipped with Cu Kα radiation. Raman spectra were captured on a Labram-1B (Dilor, France) confocal microscope Raman spectrometer with 632.8 nm incident laser light. X-ray photoelectron spectra (XPS) were obtained from a RBD upgraded PHI-5000C ESCA system (PerkinElmer, USA) with Al K radiation as the X-ray excitation source. Inductively coupled plasma atomic emission
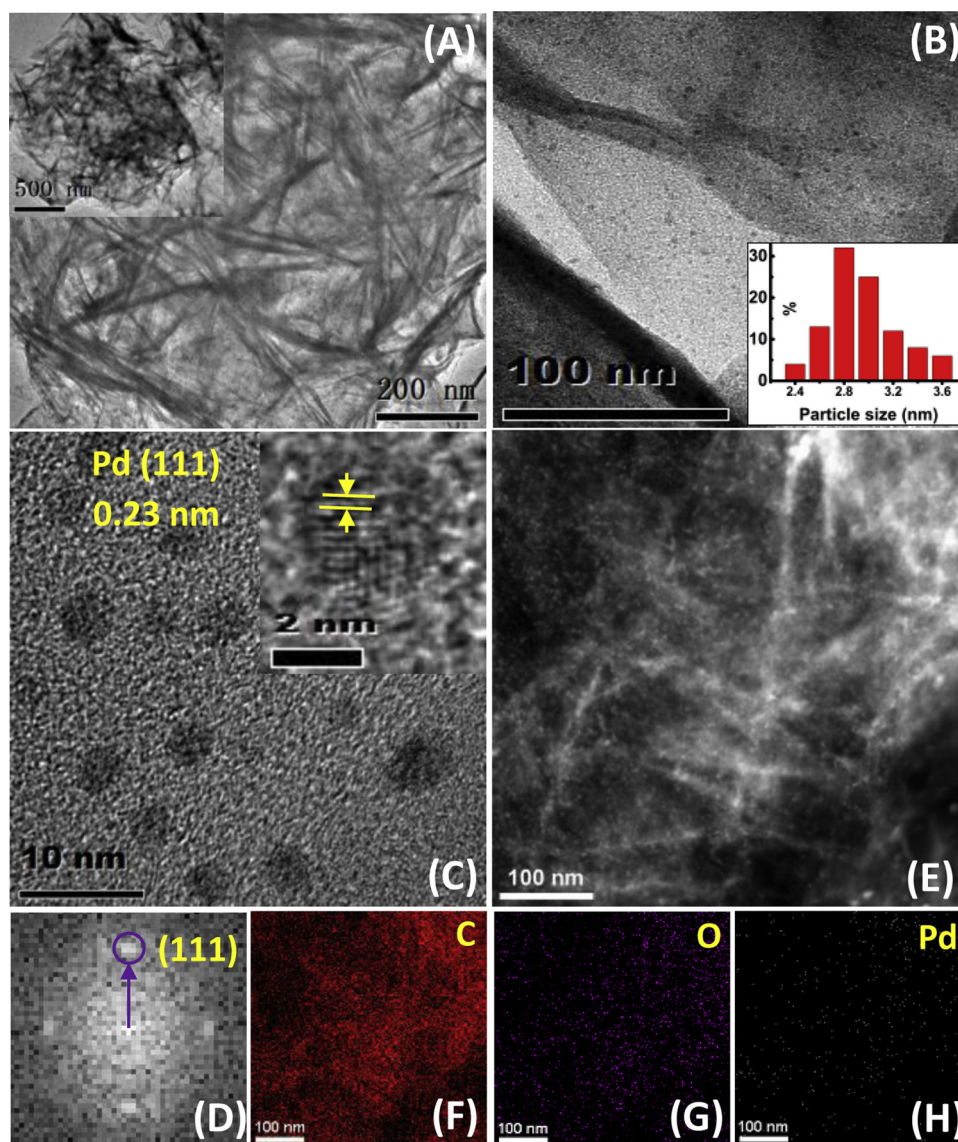
Fig. 1. (A, B) TEM images of Pd/MGN with different magnification. The inset in (B) showed the particle size distribution histogram of Pd. (C, D) HRTEM images and corresponding selected area electron diffraction pattern of Pd/MGN. The inset in (C) showed the lattice fringe of an individual Pd nanoparticle (d-spacing = 0.23 nm). (E–H) STEM image and EDX mappings of Pd/MGN.

spectrometry (ICP-AES) was measured by an Optima 8000 system (PerkinElmer, USA).

3. Results and discussion

MCM-22 is a laminar zeolite with typical layer space around 2.5 nm, which therefore can act as hard template to prepare graphene nanosheets [20]. Via optimizing the carbon filling (Experimental Section), MGN could be accordingly obtained, which exhibited a 3D-stacked ultrathin nanosheet configuration with mesocellular pores (Fig. S1). Thereafter, ultrafine Pd NPs could be well-dispersedly anchored on the MGN via a facile room temperature reduction without organic stabilizers. The as-prepared Pd/MGN inherited the 3D porous ultrathin nanosheet network of MGN (Fig. 1A and Fig. S2). Not only that, ultrafine nanoparticles (~2.8 nm) were also observed on the nanosheets (Fig. 1B), which exhibited monodispersion (Fig. 1C) and single crystalline (Fig. 1D). These nanoparticles had typical lattice space around 0.23 nm, corresponding to the (111) plane of face-centered cubic (fcc) structured Pd [21]. Meanwhile, they were well-dispersed on the mesocellular carbon matrix, exhibiting an ultrafine 3D network structure

(Fig. 1E–H). The loading amount of Pd NPs on MGN was 6.5% as measured by ICP analysis.

To have a good insight into the formation of ultrafine Pd NPs on zeolite-templated MGN, the comparative analysis between Pd/MGN and MGN was performed. As shown in Fig. 2A and Fig. S3A, Pd/MGN exhibited four extra (111), (200), (220) and (311) diffractions which could be indexed as the fcc-structured Pd, validating the presence of Pd NPs [22]. The calculated particle size (~2.92 nm) using the Scherrer formula matched well with the value measured from TEM images [23], revealing the homogeneity of the Pd NPs. Raman spectra of Pd/MGN and MGN both gave obvious signals similar to the symmetry A1g mode and E2g mode of graphitic carbon atoms at $1342\,cm^{-1}$ (D-band), $1593\,cm^{-1}$ (G-band), and $2708\,cm^{-1}$ (2D-band) (Fig. 2B and Fig. S3B), respectively, suggesting the defective graphene structure [24]. The increased I_D/I_G from 0.86 to 0.91 after Pd NPs anchoring revealed the augmented defects (disorder) due to the Pd NPs disturbing at these sites [25]. XPS spectra of Pd/MGN showed the dominated C=C signals (284.7 eV) of sp^2-hybridized graphitic carbon, accompanied by C–C (285.5 eV) and C–O (287–291 eV) signals of the defective graphene (Fig. 2D), as similar with those of MGN (Fig. S4B). Differently, Pd/MGN
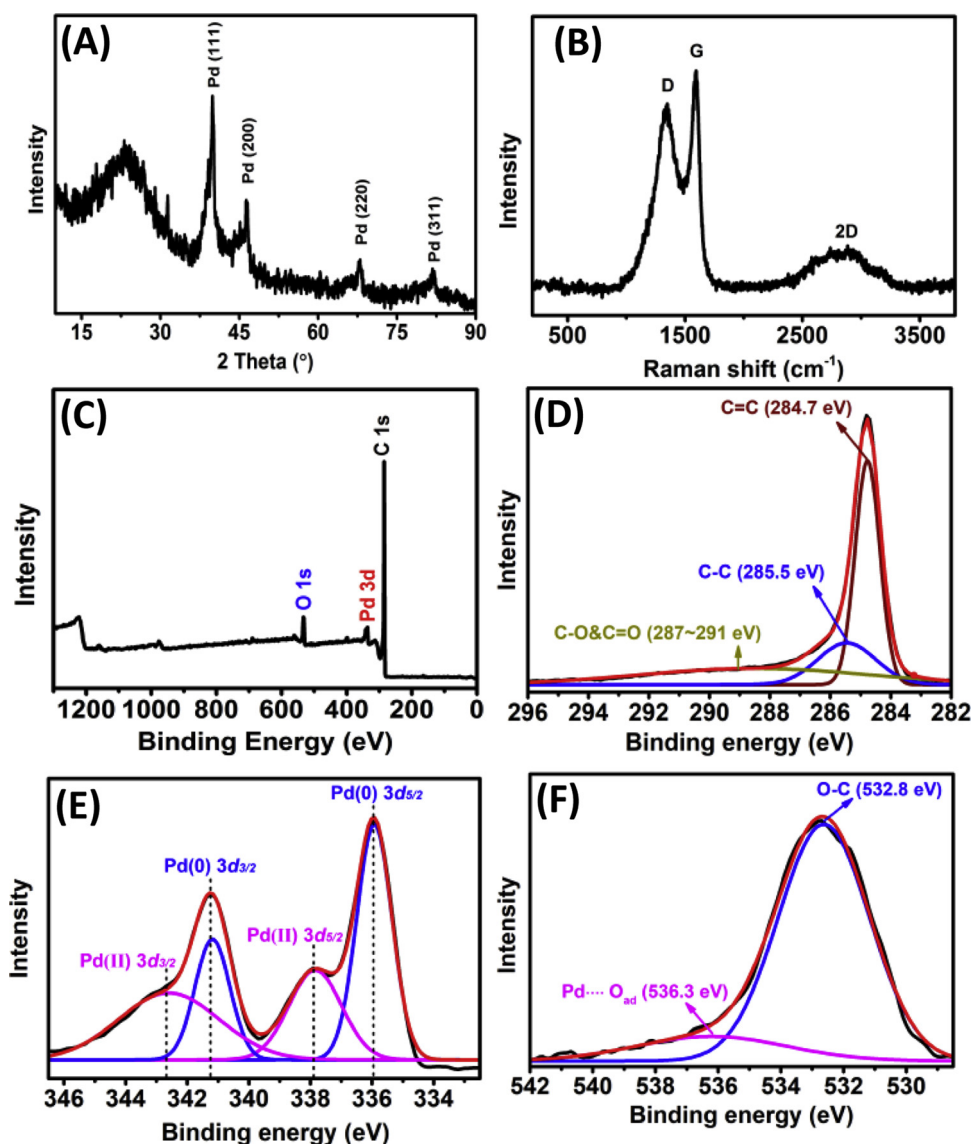
Fig. 2. XRD pattern (A), Raman spectra (B), XPS survey spectra (C) and corresponding high-resolution C 1 s (D), Pd 3d (E), and O 1 s (F) spectra of Pd/MGN.
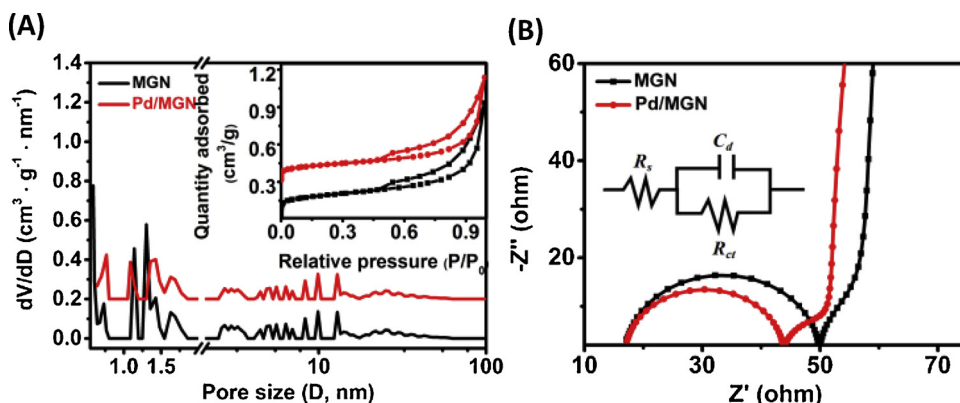

Fig. 3. (A) Pore size distribution curves and N_2 adsorption-desorption isotherms (insets) of Pd/MGN (red) and MGN (black). (B) EIS fitting curves of Pd/MGN and MGN. The inset represents the equivalent circuit of the electrode reactions consisting of solution resistance (Rs), charge-transfer resistance (Rct) and double layer capacitance (Cd) (For interpretation of the references to colour in this figure legend, the reader is referred to the web version of this article).

exhibited an extra Pd 3d signal in the survey spectra (Fig. 2C), which can be deconvoluted into two pair of well-resolved peaks indexed as the to the metallic Pd (335.9 eV & 341.2 eV) and the Pd^{2+} specie (337.9 eV & 342.7 eV) (Fig. 2E), respectively [26]. The former confirmed the anchoring of metallic Pd NPs on MGN, while the later implied the possible Pd-defect (Pd-O) mediated anchoring in the oxygen-contained

defect sites. In addition, a more obvious oxygen adsorption signal for Pd/MGN (536.3 eV) in O 1s XPS spectra (Fig. 2F) than that for MGN (Fig. S4A–C) suggested the increased oxygen adsorption sites after Pd NPs anchoring, which would be beneficial for the ORR. N_2 adsorption-desorption isotherms and pore sizes distribution curves demonstrated that MGN had a BET surface area of $698\,m^2\,g^{-1}$ and a pore volume of

$0.828\,cm^3\,g^{-1}$. After Pd loading, Pd/MGN inherited the high BET surface area ($494\,m^2\,g^{-1}$), large pore volume ($0.692\,cm^3\,g^{-1}$), and hierarchically micro-meso-macroporous framework from 3D networked MGN (Fig. 3A and Fig. S5). Herein, the macropores were originated from the network structure surrounded by the nanosheets (Fig. S2, S6). Notably, the distinct micropores ($< 2\,nm$) might originate from the defects of the templated graphene nanosheets [27]. Correspondingly, a little decreased micropore sizes in Pd/MGN as compared with MGN confirmed the anchoring of Pd NPs in the defected sites, as a result of some blockings to the micropores. Furthermore, EIS results indicated a reduced charge-transfer resistance (Rct) value from 34 Ω (MGN) to 27 Ω (Pd/MGN) (Fig. 3B), also reflecting the anchoring of Pd NPs in the defected sites, because this manner can amend the defects and consequently increase the conductivity. All these results suggested that zeolite-templated MGN was successfully prepared and can be used to dispersely anchor the ultrafine Pd NPs via a facile synthesis.

Based on the above observations together with the previous reports where $PdCl_4^{2-}$ could easily react with GO (defected graphene) to obtained Pd NPs due to the different redox potentials [28], it was speculated that zeolite framework Al templated the dispersive oxygen defects in MGN due to its Lewis acid effect (electron pair acceptor) [29], which therefore guided the formation of ultrafine Pd nanoparticles at these defect sites via the appropriate redox potentials (Scheme 1). To test this speculation, we carried XPS analysis for Al-MCM-22/MGN (Fig. S7A). It was found Al 2p can be split into two well-resolved binding states attributed to the Al-O(Al) (75.6 eV) and Al-O(C) (76.4 eV) (Fig. S7B), respectively, while Si 2p could only deconvoluted into a single binding state of Si-O(Si) (Fig. S7C). This suggested the formation of Al-O-C bonds during the templated synthesis, which would then transform into oxygen defect sites after template removal. Furthermly, a series of parallel control experiments were carried out to prove the key effect of zeolite Al. First, dealuminated MCM-22 (28% Al removal via acid washing) and aluminum-free silica spheres were used to template the porous carbon, on which Pd NPs were then anchored using the same procedure. As shown in Fig. 4B, the density of Pd NPs on the dealuminated MCM-22 templated nanosheets was apparently decreased. And also, few nanoparticles were observed on the margins of silica sphere-templated carbon (Fig. 4C). These suggested the decreased or only the marginal oxygen defect sites in dealuminated MCM-22 and aluminum-free silica spheres templated carbon, respectively, which consequently contributed to the less densities of Pd NPs than that on MGN via the defects-mediated reduction (Fig. 4A). Second, oxidized graphene (GO) with different degrees of thermal reduction was used to anchor Pd NPs. As shown in Fig. 4D–F, Pd NPs on GO were not well uniformed with much bigger size (2–32 nm) than those in Pd/MGN, and some of them were fused into Pd nanosheets. This might be attributed to the superfluous and inhomogeneous oxygen defect sites in GO, which guided the overgrowth and amalgamations of Pd NPs. Therefore, with the decrease of oxygen defect sites, Pd NPs with gradually decreased size and increased uniformity were observed on the thermally reduced GO. However, a desirable Pd/graphene catalyst with large surface area and ultrafine Pd NPs was difficult to be obtained via this stabilizer-free

synthesis due to the thermal-induced aggregation of nanosheets and uncontrollability of defects, respectively. At last, both pristine and oxidized MWCNT were also exploited to anchor the Pd NPs. The former is lack of defects so that only few Pd NPs formed on the wrinkled sites (Fig. 4G). In contrast, large Pd NPs, even the Pd nanowires, were observed to grow along the surfaces of the oxidized MWCNTs due to the abundant and dense surface oxidation defects (Fig. 4H). All these results illuminated that MGN could be templated by zeolite MCM-22, where its framework Al acted as Lewis acid to induce the defect sites. Consequently, ultrafine Pd NPs can be formed and dispersedly anchored on the MGN via the defect-mediated reduction. The hierarchically porous structure with the ultrafine Pd NPs made Pd/MGN a promising electrocatalyst, which was evaluated as follows.

Initially, the catalytic ORR activities of Pd/MGN were examined and compared with those of MGN and commercial Pt/C (20 wt% Pt) catalysts. As shown by cyclic voltammetry curves in Fig. 5A, Pd/MGN exhibited obvious cathodic reduction peaks at about -0.2 V in O_2 saturated 0.1 M KOH aqueous solution but not any redox peaks at this potential in the N_2 saturated electrolyte, suggesting the ORR activity on Pd/MGN catalyst [30]. Furtherly, the polarization curves displayed the diffusion-limiting current region from -0.02 to -0.25 V and the mixed kinetic-diffusion control region between -0.3 and -0.7 V (Fig. 5B). The onset potential (-0.026 V), half-wave potential (-0.118 V) and the diffusion-limiting current density of Pd/MGN were all higher than those of MGN and commercial Pt/C catalysts as well as the other counterparts (Fig. 5C and Fig. S8), indicating that Pd/MGN possessed best electrocatalytic activity toward ORR even with low Pd loading. Correspondingly, the mass current density normalized by metal was $608.2\,mA\,mg_{Pd}^{-1}$ for Pd/MGN, 3.6 times than that of the commercial Pt/C catalyst ($169.2\,mA\,mg_{Pt}^{-1}$), revealing the ultrahigh Pd utilization efficiency. The current densities of Pd/MGN steadily augments with increasing rotation speeds due to the shortened diffusion distance. As a result, they exhibited almost overlapping linear Koutecky-Levich (K–L) plots at different potentials from -0.2 to -0.7 V (Experimental Section), reflecting a good first-order reaction with respect to the dissolved O_2 (Fig. 5B) [31]. Accordingly, the electron transfer numbers were calculated to be 4.1–4.3 at this potential ranging [32], suggesting the 4 e^- ORR process on Pd/MGN electrode (Fig. 5C). This kinetic process was similar with that on Pt/C electrode (4 e^-) (Fig. S9E), but faster than that on MGN electrode (3.5 e^-) (Fig. S9F), revealing the enhanced catalytic activity via Pd NPs anchoring. The excellent ORR activity with quick reaction kinetics of the Pd/MGN catalyst was further proved by the smaller Tafel slope of 61 mV dec^{-1} than that of Pt/C (90 mV dec^{-1}) at low polarization region [33]. Notably, the value was approximately equal to that of MGN (63 mV dec^{-1}) (Fig. 5D), implying that the hierarchical porous structure of MGN made a significant contribution to the mass and electron transfer because of its high diffusivity.

Next, the durability of Pd/MGN catalyst was evaluated by a standard accelerated durability test (ADT) for 1000 cycles. As shown in Fig. 5E, both the onset potential and the half-wave potential of Pd/MGN had slightly positive shifts about 10 mV and 3 mV, respectively, after 1000 continuous cycles. These were much more superior to those
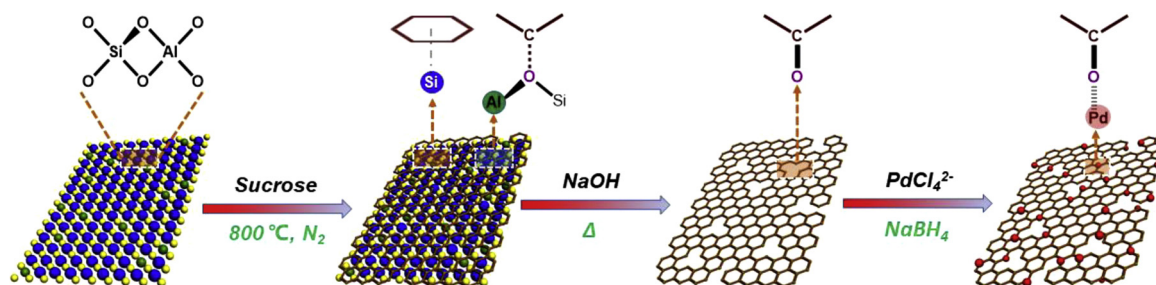
Scheme 1. Illustrated formation of MGN using zeolite MCM-22 as template and the corresponding framework Al effect on the growth of ultrafine Pd nanoparticles. The MCM-22 nanosheets is simplified as flat without illustration of bond angles.
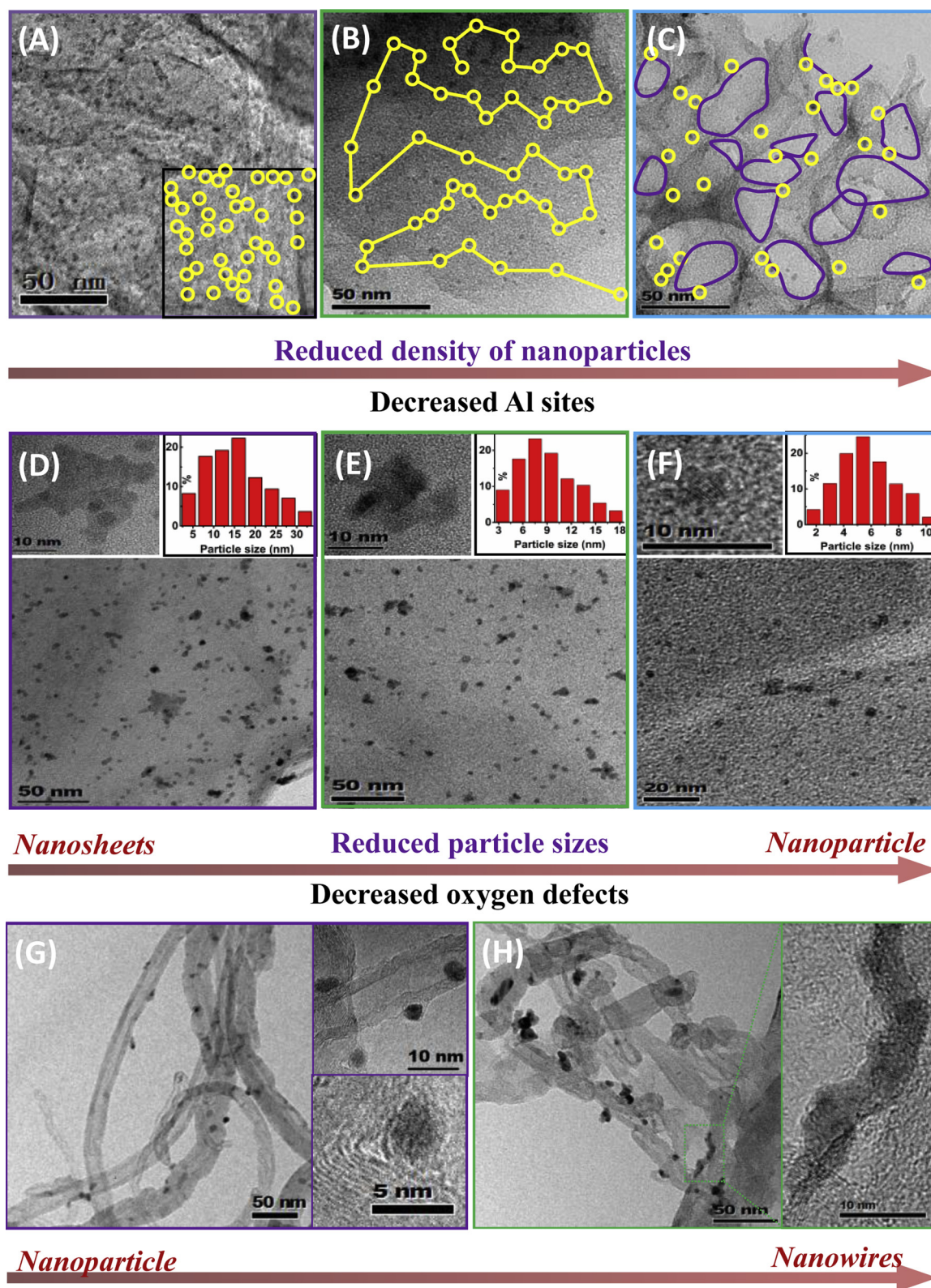
Fig. 4. (A–C) TEM images of Pd NPs (yellow circle) supported on carbon templated by zeolite MCM-22, dealuminated zeolite MCM-22, and pristine silica spheres, respectively. The yellow lines showed the spaces (an average of 13 nm) between the particles, and the purple circles highlighted the pores templated by silica nanospheres. (D–F) TEM images, HRTEM images and corresponding particle size distribution of Pd NPs supported on GO, reduced GO at 200 ℃, and reduced GO at 800 ℃, respectively. (G, H) TEM and HRTEM images of Pd NPs supported on pristine MWCNT and oxidized MWCNT, respectively (For interpretation of the references to colour in this figure legend, the reader is referred to the web version of this article).
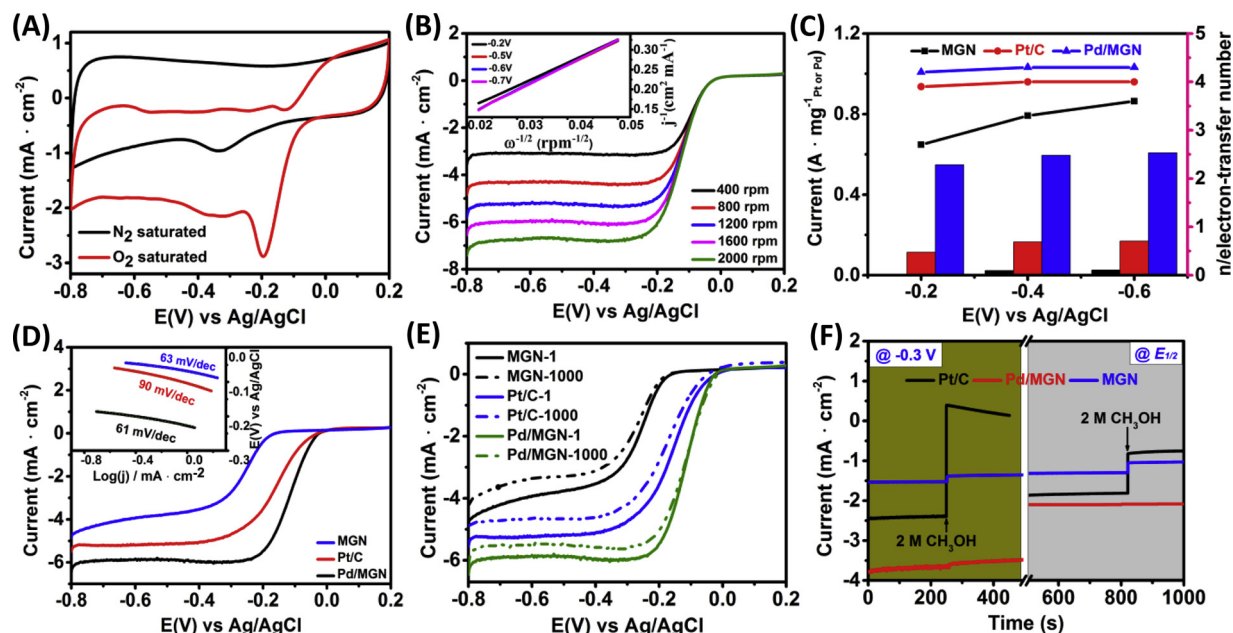
Fig. 5. (A) CV curves of Pd/MGN in N_2 and O_2 saturated 0.1 M KOH aqueous solutions at a scan rate of 50 mV s^{-1}. (B) LSV curves of Pd/MGN at different rotating rates in O_2 saturated 0.1 M KOH electrolyte at a scan rate of 10 mV s^{-1}. Inset: the corresponding Koutecky-Levich plots at different potentials. (C) Comparison of the mass activity of MGN (A mg^{-1}), Pd/MGN (A mg$_{Pd}^{-1}$) and commercial Pt/C (A mg$_{Pt}^{-1}$) catalysts and the corresponding electron-transfer number (n) on basis of the RDE data at different potentials (-0.2 V, -0.4 V and -0.6 V). (D) LSV curves and the corresponding Tafel plots (inset) of various catalysts at a rotation rate of 1600 rpm. (E) LSV curves before and after 1000 cycles in 0.1 M KOH at a scan rate of 50 mV s^{-1} for the Pd/MGN, MGN and Pt/C, respectively. (F) Chronoamperometric response of the various catalysts in O_2 saturated 0.1 M KOH solution at -0.3 V and $E_{1/2}$. The arrows indicated the addition of 2 M methanol.

Table 1
Comparisons of electrochemical performances of different catalysts calculated from the electrochemical measurements.

	E_{onset}/mV		$E_{1/2}$/mV		j/mA cm^{-2}					
					@$E_{1/2}$		@-0.2V		@-0.4V	
	C_1	Δ	C_1	Δ	C_1	Δ%	C_1	Δ%	C_1	Δ%
MGN	−163	−6	−277	−12	−2.29	12.9	−0.36	38.5	−3.52	11.9
Pt/C	−35	−17	−169	−25	−2.61	9.1	−3.48	21.8	−5.06	10.1
Pd/MGN	−26	10	−118	3	−3.08	5.6	−5.47	8.2	−5.97	6.2

C_1: the first cycle; C_{1000}: the thousandth cycle; Δ: C_{1000}-C_1; Δ%: (C_{1000}-C_1)/C_1.

negative shifts of MGN and Pt/C catalysts (Table 1), indicating the enhanced catalytic activity of Pd/MGN after ADT. The desirable property is probably due to the hydrophobic nature of the MGN support so that it required some time to allow O_2 molecules and the aqueous electrolyte to diffuse into and wet the active sites for promoting the catalytic activity [34]. Moreover, the current densities of Pd/MGN at different potentials only decreased by 5.6%–8.2% after ADT, which were much lower than those of MGN (11.9%–38.5%) and Pt/C (9.1%–21.8%) catalysts at the same test, verifying the high stability of Pd/MGN. In addition, XPS results of Pd/MGN after 1000 cycles gave much more obvious Pd(II)-O peaks than those of Pd/MGN (Fig. S10), suggesting some inevitable surface oxidation to the metal during the ADT test. Nevertheless, the reserved sp^2-hybridized graphitic carbon with the dominated C=C signals accompanied by C−C and C−O signals, and also the main metallic Pd with some Pd^{2+} species for Pd/MGN-1000 (Fig.S10B-D and Fig. 2C−F), still suggested the good stability of Pd/MGN during the ADT test. Herein, the F-related signals in the XPS spectra of Pd/MGN-1000 came from the adsorbed nafion during the electrode preparation.

Finally, the methanol tolerance was also tested by methanol-crossing chronoamperometric curves. As shown in Fig. 5F, commercial Pt/C exhibited two sharp current decreases at both the half-wave potential and the diffusion current potential (−0.3 V) due to its advanced

MOR ability at a wide potential, and MGN also displayed two slightly current decays possibly owing to the interference of the adsorbed methanol toward the catalytic active sites of MGN [35]. On the contrary, Pd/MGN exhibited negligible current decreases at especially the half-wave potential, suggesting the high electrocatalytic selectivity toward ORR without noticeable activity for MOR at this potential. This methanol tolerant ORR is favored for developing DMFCs because more methanol can be fed at the anode and the poisoning effect could be mitigated at the cathode.

All these results revealed the advanced ORR electrocatalyst of Pd/MGN, whose activity and durability were also much superior to those of many other reported Pd-based catalysts (Table S1). The good catalytic performances could be attributed to: (1) zeolite-templated graphene network with hierarchically porous structure and large surface area, which was beneficial for the mass transfer (O_2 diffusion and −OH desorption); (2) Pd NPs-amended graphene-like framework with high conductivity, which was favored to the fast electron transfer; (3) highly dispersive and ultrafine Pd NPs, which was useful to break the O−O bonds for the enhanced activity with plentiful active sites [36]; (4) zeolite Al-templated defects, benefiting a lot to anchor Pd NPs with promoted catalytic stabilization; and (5) hydrophobic rendering of MGN to methanol, which may account for the advanced methanol-tolerant behavior [34,37]. In addition, originating from the unique

structure and advanced properties, Pd/MGN can also be explored as the oxygen evolution reaction (OER) electrocatalyst, which exhibited better catalytic activity than commercial Pt/C and even the state-of-the-art RuO₂ (Fig. S11). Although the detailed OER performances are still under the research, the facile synthesis and the advanced ORR ability of Pd/MGN promised a feasible catalyst for highly efficient catalytic applications.

4. Conclusions

In summary, MGN with hierarchically porous structure was synthesized using zeolite MCM-22 as template. The zeolite framework Al was found to contribute to MGN with optimal oxygen defects, which were therefore used for anchoring the ultrafine and dispersive Pd NPs to get Pd/MGN catalyst with large surface area and high conductivity. This catalyst exhibited advanced ORR catalytic activity and durability due to the elaborated structure, whose onset potential, half-wave potential and limiting-diffusion current density before and after ADT tests were all much more superior to those of commercial Pt/C catalyst and its counterpart MGN. Moreover, Pd/MGN demonstrated advanced methanol-tolerant behavior and also the significant OER activity due to the unique structure and advanced properties. As a result, this work presented an elaborative insight into zeolite-templated carbon for Pd NPs anchoring, and consequently provides a facile method to prepare cost-effective and highly efficient Pd-based electrocatalyst for sustainable energy applications.

Acknowledgments

References

[1] C. Meng, T. Ling, T.Y. Ma, H. Wang, Z.P. Hu, Y. Zhou, J. Mao, X.W. Du, M. Jaroniec, S.Z. Qiao, Adv. Mater. 29 (2017) 1604607.
[2] W. Ding, M.R. Xia, Z.D. Wei, S.G. Chen, J.S. Hu, L.J. Wan, X.Q. Qi, X.H. Hu, L. Li, Chem. Commun. 50 (2014) 6660–6663.
[3] S.Y. Ma, H.H. Li, B.C. Hu, X. Cheng, Q.Q. Fu, S.H. Yu, J. Am. Chem. Soc. 139 (2017) 5890–5895.
[4] P.Z. Chen, T.P. Zhou, L.L. Xing, K. Xu, Y. Tong, H. Xie, L.D. Zhang, W.S. Yan, W.S. Chu, C.Z. Wu, Y. Xie, Angew. Chem. Int. Ed. 56 (2017) 610–614.
[5] M.R. Xia, W. Ding, K. Xiong, L. Li, X.Q. Qi, S.G. Chen, B.S. Hu, Z.D. Wei, J. Phys. Chem. C 117 (2013) 10581–10588.
[6] G. WU, P. Zelenay, Acc. Chem. Res. 46 (2013) 1878–1889.
[7] X.X. Yan, K.X. Liu, T. Wang, Y. You, J.G. Liu, P. Wang, X.Q. Pan, G.F. Wang, J. Luo, J. Zhu, J. Mater. Chem. A 5 (2017) 3336–3345.
[8] Z.H. Sheng, L. Shao, J.J. Chen, W.J. Bao, F.B. Wang, X.H. Xia, ACS Nano 5 (2011) 4350–4358.
[9] Y.Y. Liang, Y.G. Li, H.L. Wang, J.G. Zhou, J. Wang, T. Regier, H.J. Dai, Nat. Mater. 10 (2011) 780–786.
[10] L. Chen, L.L. Lu, H.L. Zhu, Y.G. Chen, Y. Huang, Y.D. Li, L.Y. Wang, Nat. Commun. 8 (2017) 14136.
[11] L.L. Zhang, Q.W. Chang, H.M. Chen, M.H. Shao, Nano Energy 29 (2016) 198–219.
[12] Y.P. Zuo, D.W. Rao, S. Li, T.T. Li, G.L. Zhu, S.M. Chen, L. Song, Y. Chai, H.Y. Han, Adv. Mater. 30 (2018) 1704171.
[13] L.L. Zhang, S.Q. Zhu, Q.W. Chang, D. Su, J. Yue, Z. Du, M.H. Shao, ACS Catal. 6 (2016) 3428–3432.
[14] S.P. Li, J.P. Lai, R. Luque, G.B. Xu, Energy Environ. Sci. 9 (2016) 3097–3102.
[15] Y. Qin, L. Chao, J. Yuan, Y. Liu, F.Q. Chu, Y. Kong, Y.X. Tao, M.L. Liu, Chem. Commun. 52 (2016) 382–385.
[16] S.J. Guo, S.J. Dong, E.K. Wang, ACS Nano 4 (2010) 547–555.
[17] W. Wang, Z.Y. Wang, J.J. Wang, C.J. Zhong, C.J. Liu, Adv. Sci. 4 (2017) 1600486.
[18] M.C. Wen, K. Mori, Y. Kuwahara, H. Yamashita, ACS Energy Lett. 2 (2017) 1–7.
[19] Y.H. Han, Y.G. Wang, W.X. Chen, R.R. Xu, L.R. Zheng, J. Zhang, J. Luo, R.A. Shen, Y.Q. Zhu, W.C. Cheong, C. Chen, Q. Peng, D.S. Wang, Y.D. Li, J. Am. Chem. Soc. 139 (2017) 17269–17272.
[20] Y. Wang, H. Sun, R. Zhang, S.N. Yu, J.L. Kong, Carbon 53 (2013) 245–251.
[21] J.N. Tiwari, W.G. Lee, S. Sultan, M. Yousuf, A.M. Harzandi, V. Vij, K.S. Kim, ACS Nano 11 (2017) 7729–7735.
[22] Z. Xi, D.P. Erdosy, A.M. Garcia, P.N. Duchesne, J.R. Li, M. Muzzio, Q. Li, P. Zhang, S.H. Sun, Nano Lett. 17 (2017) 2727–2731.
[23] K.A. Aly, N.M. Khalil, Y. Algamal, Q.M.A. Saleem, J. Alloys Compd. 676 (2016) 606–612.
[24] X. Zhang, J.X. Zhu, C.S. Tiwary, Z.Y. Ma, H.J. Huang, J.F. Zhang, Z.Y. Lu, W. Huang, Y.P. Wu, ACS Appl. Mater. Interfaces 8 (2016) 10858–10865.
[25] L. Ye, G.L. Chai, Z.H. Wen, Adv. Funct. Mater. 27 (2017) 1606190.
[26] N. Ullah, M. Imran, K. Liang, C.Z. Yuan, A. Zeb, N. Jiang, U.Y. Qazi, S. Sahar, A.W. Xu, Nanoscale 9 (2017) 13800–13807.
[27] J. Zhao, Y.F. Jiang, H. Fan, M. Liu, O. Zhuo, X.Z. Wang, Q. Wu, L.J. Yang, Y.W. Ma, Z. Hu, Adv. Mater. 29 (2017) 1604569.
[28] X.M. Chen, G.H. Wu, J.M. Chen, X. Chen, Z.X. Xie, X.R. Wang, J. Am. Chem. Soc. 133 (2011) 3693–3695.
[29] J.W. Harris, M.J. Cordon, J.R.D. Iorio, J.C.V. Vila, F.H. Ribeiro, R. Gounder, J. Catal. 335 (2016) 141–154.
[30] Z.Y. Zhang, S.S. Liu, X. Tian, J. Wang, P. Xu, F. Xiao, S. Wang, J. Mater. Chem. A 5 (2017) 10876–10884.
[31] H. Jiang, Y.Q. Wang, J.Y. Hao, Y.S. Liu, W.Z. Li, J. Li, Carbon 122 (2017) 64–73.
[32] J.N. He, B.B. Li, J. Mao, Y.Q. Liang, X.J. Yang, Z.D. Cui, S.L. Zhu, Z.Y. Li, J. Mater. Sci. 52 (2017) 10938–10947.
[33] Y. Zheng, Y. Jiao, Y.H. Zhu, Q.R. Cai, A. Vasileff, L.H. Li, Y. Han, Y. Chen, S.Z. Qiao, J. Am. Chem. Soc. 139 (2017) 3336–3339.
[34] Z.X. Wu, Y.Y. Lv, Y.Y. Xia, P.A. Webley, D.Y. Zhao, J. Am. Chem.Soc. 134 (2012) 2236–2245.
[35] J.C. Yang, S.H. Kim, S.K. Kwak, H.K. Song, ACS Appl. Mater. Interfaces 9 (2017) 23302–23308.
[36] W. Wang, Z.Y. Wang, J.J. Wang, C.J. Zhong, C.J. Liu, Adv. Sci. 4 (2017) 1600486.
[37] W.C. Choi, S.I. Woo, M.K. Jeon, J.M. Sohn, M.R. Kim, H.J. Jeon, Adv. Mater. 172 (2005) 446–451.